Optimization-Based Estimation and Model Predictive Control for High Performance, Low Cost Software-Defined Power Electronics

Liwei Zhou, *Member, IEEE*, Michael Eull, *Member, IEEE*, Matthias Preindl, *Senior Member, IEEE*

***Abstract*—A combined optimization-based estimation (OBE)-model predictive control (MPC) technique is developed to improve the dynamic performance of a reconfigurable LC-based power module with lower cost, less noise/oscillation. The developed OBE-MPC technique and the corresponding power module is based on a software-defined power electronics concept which can be reconstructed as different topologies and applied to various load/source applications, e.g., DC/DC converters, DC/AC single/three-phase grid-connected inverters and DC/AC motor traction inverter to improve the energy conversion performance. The software-defined power electronics is designed in a generalized way by manipulating different number of OBE-MPC power modules with holistic high level control functions for wide applications. Symmetrically mirrored to the MPC, the OBE is configured as a constrained finite time optimal estimation (CFTOE) problem to solve the quadratic cost function based on the past sampling information. With the designed OBE, the sensor count is reduced with less noise/oscillation. And the highly accurate OBE contributes to the correction of possible modeling parametric or sampling errors. The integration of OBE-MPC algorithms improves both the steady state and dynamic performances with less noise/oscillation, more robust transient behavior and higher control bandwidth. The explicit design of OBE-MPC algorithms makes it possible to implement the functions on a low cost DSP. Also, the state space modeling of OBE-MPC for the LC-based power module is immune to the output side unknown inductance which further improves the parametric accuracy. The proposed methods have been validated experimentally.**

***Index Terms*—Optimization-based estimation, model predictive control, software-defined power electronics, dynamic performance, grid-connection, motor drives.**

I. Introduction

THE power quality, dynamic performance and cost of the power converters are three key aspects for the evaluation of an energy conversion system. For the power quality, a high order filter, such as LC or LCL, can be applied to the converter to filter out the harmonics. However, there exists resonance oscillation in high order filter system which could result in stability issue. Some passive/active damping techniques have been studied to deal with the resonance by either introducing extra passive components or adding extra ADC sampling information with the corresponding integral calculation into the control loop. For the dynamic performance, higher control bandwidth or more advanced control techniques could contribute to the improvement of transient behavior. However, higher control bandwidth requires more cost on the controller's computation capability. Advanced control methods, such as MPC, can also promote the dynamic performance. However, MPC is typically implemented based on solving the constrained optimization problem which may still require more computation resources. For the cost reduction of power converters, sensorless control is one of the most straightforward ways to save components on the sensor count and reduce the related hardware cost.

State estimator is a typical technique to improve the power quality and reduce the cost for power converters [1], [2]. In a power electronics system, the voltage/current samplings are crucial parameters that could directly influence the performance of power control. Due to the hardware limitations, e.g., EMI noise from the high power traces, measurement error, of the sensing circuits, the control system could be interfered by the sampling noise or oscillation. The state estimation can be a substitute for part of the ADC sampling information to reduce the noise/oscillation from the corresponding sensors [3], [4]. Also, the state estimation contributes to the reduction of sensor count and system cost. Conventionally, the Luenberger Observer is a basic state estimation method and has been widely used in the industry applications which is a linear type of observer and can be easily implemented in the digital control systems [5], [6]. Besides the Luenberger Observer, optimization-based estimation (OBE) is a more advanced estimation approach that leverages a series of past measurements to derive the desired accurate state values by solving a constrained optimization problem [7], [8]. The OBE has been verified for the application of virtual flux estimation in electric machine to estimate the position and speed [9]–[11]. Few studies have been focusing on the applications of different topologies to be interfaced with wider ranges of load/source. Also, the computation burden for the OBE on low cost DSP is a crucial topic that needs to be addressed for the popularization of the technique. This paper develops a general explicit OBE-MPC method for power modules that could be applied to various types of power converters with different load/source interfaces on a low cost DSP.

Model predictive control (MPC) is an option for the promotion of dynamic performance and resonance damping, especially in high order filter system [12]–[14]. Different from the conventional proportional-integral (PI) control, the MPC has been validated to have the advantages of better dynamic performance, including less rise time, overshoot and oscillation during transient [15], [16]. [17] demonstrated the applications of predictive control method with the corresponding merits of switching frequency reduction and output distortion attenuation. Also, three perspectives of conclusions have been drawn

in this paper including: (1) MPC can derive the optimal results at low switching frequency range; (2) high frequency state variable sampling updates are not necessary for predictive control; (3) complicated modeling is not necessary for predictive control. Several MPC algorithms have been studied in the field of power converters for motor traction or grid-connection [18]–[21]. However, the combination of MPC and OBE for a general application and low cost implementation purposes have not been addressed in details. The MPC and OBE are actually two symmetrical algorithms in the time series where OBE is focusing on the past sampling information and MPC is for the future steps. This paper integrates the OBE and MPC on a generalized power module which could be applied to various interfaced applications without consuming high computation burden on the controller.

For the modularization concept, power electronics building block (PEBB) has been proposed to standardize the hardware components for stackable energy conversion systems [22]–[24]. The PEBB concept is more focusing on the physical components design to generalize the hardware power modules with extensible voltage/current capacity. Accordingly, in a PEBB system, the number of power blocks are mainly targeting for the desired power rating instead of various interfaced applications. On the contrary, some studies have also developed power electronics control architectures in a high level perspective to cover various applications [25]–[28]. This type of idea addresses more on the holistic interfaced control functions. The software-defined power electronics concept in this paper basically combines the characteristics of hardware stackability and software reconfigurability. For the hardware stackability, the generalized power module can be physically connected in parallel for desired power rating based on the inspiration of PEBB concept. For the software reconfigurability, the high level controller can manage the desired number of power modules with the corresponding control functions based on the interfaced applications. And the OBE and MPC algorithms are configured for each local controller to estimate and stabilize the state variables. The local controller is necessary for implementing the OBE and MPC in each module since it is difficult to execute the optimization-based algorithms in a holistic way especially when the interfaced applications require a multi-phase circuitry topology.

The contributions of this paper can be summarized in four aspects: (1) OBE-MPC algorithms are designed for a reconfigurable LC-based power module; (2) a software-defined multi-layer control structure is developed with high level control functions and local level OBE-MPC power modules; (3) three types of interfaced applications have been validated including DC/DC, single/three-phase DC/AC grid and motor traction; (4) the proposed control and estimation methods show high performances in steady state and transient modes.

This paper is organized as follows. Firstly, the state space modeling of an LC-based power module is analyzed for the implementation of OBE-MPC as the generalized module of the software-defined power electronics. Secondly, the explicit OBE-MPC algorithms are designed with the corresponding general theories and implementation details. Also the explicit working principle for reducing the computation burden on low cost DSP has been illustrated. Thirdly, based on the developed OBE-MPC equipped power module, various types of topologies and interfaced applications including DC/DC converters, DC/AC single/three-phase grid-connected inverters and motor traction inverter are demonstrated with the corresponding control diagrams based on the generalized software-defined power electronics concept. Finally, the proposed OBE-MPC technique for different applications has been experimentally validated to show the merits.

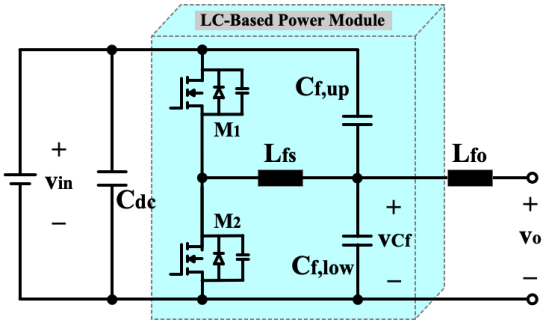

Fig. 1. LC-based power module with output side inductor.

II. State Space Modeling

The state space modeling of the LC-based power module is analyzed in this section. The circuitry diagram of the basic LC power module is shown Fig. 1 which consists of upper/lower switches, M_1 and M_2, switch side inductor, L_{fs}, upper/lower output capacitors, $C_{f,up}$ and $C_{f,low}$. An output side inductor, L_{fo}, can also be connected to formulate an LCL converter. The desired number of introduced basic LC-based power modules can be connected and reconfigured to formulate different types of topological applications such as multi-phase DC/DC or DC/AC converters.

The state space equations for the LC-based power module can be expressed as:

$$\dot{i}_{Lfs}(t) = -\frac{1}{L_{fs}} v_{Cf}(t) + \frac{v_{in}}{L_{fs}} d(t) \tag{1a}$$

$$\dot{v}_{Cf}(t) = \frac{1}{C_f} i_{Lfs}(t) - \frac{1}{C_f} i_{Lfo}(t). \tag{1b}$$

$$\dot{i}_{Lfo}(t) = \frac{1}{L_{fo}} v_{Cf}(t) - \frac{1}{L_{fo}} v_o(t). \tag{1c}$$

where L_{fs}, C_f and L_{fo} are the switch side inductor, output capacitor and output side inductor, respectively. i_{Lfs}, v_{Cf}, i_{Lfo} and v_o are the switch side inductor current, output capacitor voltage, output side current and output voltage.

For the convenience of implementing the control algorithm in a low cost DSP, the continuous state space equations can be transformed into discrete format as is shown below:

This article has been accepted for publication in IEEE Transactions on Power Electronics. This is the author's version which has not been fully edited and content may change prior to final publication. Citation information: DOI 10.1109/TPEL.2022.3202863

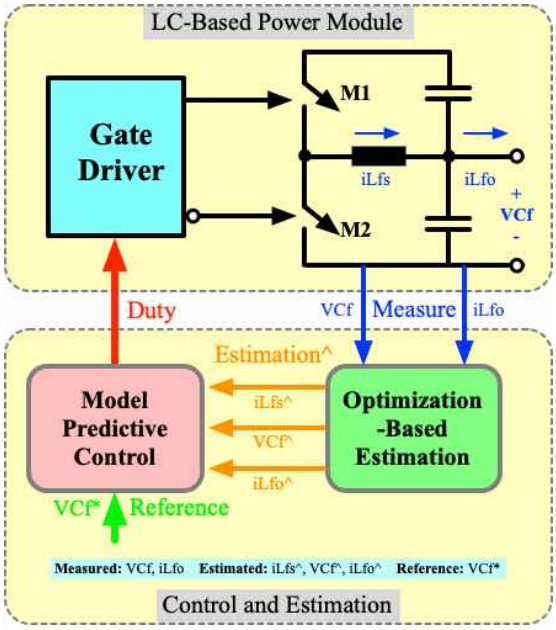

Fig. 2. OBE-MPC control diagram of LC-based power module.

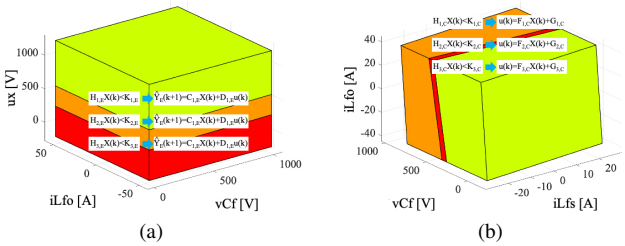

(a) (b)

Fig. 3. (a) OBE and (b) MPC partitions for explicit implementations in DSP.

$$i_{Lfs}(k+1) = i_{Lfs}(k) - \frac{T_s}{L_{fs}} v_{Cf}(k) + \frac{v_{dc} T_s}{L_{fs}} d(k) \quad (2a)$$

$$v_{Cf}(k+1) = \frac{T_s}{C_f} i_{Lfs}(k) + v_{Cf}(k) - \frac{T_s}{C_f} i_{Lfg}(k) \quad (2b)$$

$$i_{Lfo}(k+1) = i_{Lf0}(k) + \frac{T_s}{L_{fo}} v_{Cf}(k) - \frac{T_s}{L_{fo}} v_o(k) \quad (2c)$$

where T_s represents the time period of control interrupt in the DSP. The OBE-MPC algorithms are designed based on the discrete-time state space modeling of the basic LC type of power module to formulate different applications of converter, e.g., single/three-phase DC/AC inverters, multi-phase DC/DC converters.

III. Estimation and Control

The proposed integrated optimization-based estimation and model predictive control (OBE-MPC) method for LC-based power module is analyzed in this section. These two advanced techniques are all configured by solving the constrained finite time optimization problems to increase the modeling/sampling accuracy, reduce the hardware cost, enhance the anti-noise capability and improve the steady state/dynamic performances. These two techniques, OBE and MPC, are integrated based on a monolithic state space model of LC power module by dealing with two sets of ADC sampling data. The two sets of sampling data for OBE and MPC are symmetric in time sequences for the past and future, respectively.

A. Optimization-Based Estimation

Different from the traditional Luenberger observer, optimization-based estimation is designed to solve a constrained finite time optimal estimation problem that requires a sequence of past sampling information. The general theory and the implementation for the LC-based power module are analyzed in this section.

1) General Theory of OBE: For the general applications of OBE in power converters, a theoretical model for the state-space system should be firstly built in a general way as follows:

$$x(k+1) = f(x(k), u(k)) + e_p(k) \quad (3a)$$

$$y(k+1) = g(x(k)) + e_m(k) \quad (3b)$$

where $x(k) \in \mathcal{X} \subseteq \mathbb{R}$ is the state variable vector, $u(k) \in \mathcal{U} \subseteq \mathbb{R}$ is the input variable vector, $y(k) \in \mathcal{Y} \subseteq \mathbb{R}$ represents the output variable vector, $e_p(k) \in \mathcal{E}_p \subseteq \mathbb{R}$ is the unknown processing disturbance and $e_m(k) \in \mathcal{E}_m \subseteq \mathbb{R}$ is the unknown measurement noise.

The OBE algorithm is derived by solving the constrained finite time optimal estimation (CFTOE) problem. Thus, based on the general state space equations in (3), a cost function can be configured to optimize the estimation values of state variable vector, $x(k)$, by leveraging a series of past measurement of output variable vector, $y(k)$. The cost function can be generally expressed as:

$$\underset{\hat{x}(M),\ldots,\hat{x}(0)}{\operatorname{argmin}} \sum_{k=M}^{-1} e_{p,k}^T \mathbf{Q}_E e_{p,k} + \sum_{k=M}^{0} e_{m,k}^T \mathbf{R}_E e_{m,k} + e_{x,M}^T \mathbf{P}_E e_{x,M}. \quad (4)$$

And the constraints are followed by:

$$s.t. \quad e_{p,k} = f(\hat{x}(k), u(k)) - \hat{x}(k+1) \in \mathcal{E}_p \quad (5a)$$

$$e_{m,k} = g(\hat{x}(k)) - y(k) \in \mathcal{E}_m \quad (5b)$$

$$e_{x,k} = \hat{x}_M - x(E) \quad (5c)$$

$$\hat{x}(k) \in \mathcal{X} \quad (5d)$$

where $k < 0$ in (4) and (5) means the information derived from the past instants. The weighing matrices, $\mathbf{Q}_E$ and $\mathbf{R}_E$, provide the penalties on processing disturbance and measurement noise, respectively. The matrix, $\mathbf{P}_E$, is defined as the arrival cost which is a basic term in OBE that connects the properties between the finite time estimators and the full information observers. The arrival cost term is used to summarize the past data which have not been explicitly taken into account in the cost function. Also the arrival cost term is leveraged to make sure of the stability, robustness and convergence.

2) Implementation of OBE for LC-Based Power Module: The OBE method is applied to the LC-based power module for the optimal estimation. Considering the huge current ripple on the switch side inductor current measurement, i_{Lfs}, and the challenges to accurately sample the averaged i_{Lfs},the optimization-based estimator (OBE) is designed for per phase power module to provide more accurate switch side inductor current estimation and noise rejection for the MPC controller. The main purposes of the state estimator are (1) avoid inaccuracy of inductor current sampling with high current ripple; (2) improve the anti-noise capability for better control performance; (3) reduce the sensor cost.

The OBE is implemented by solving the *Constrained Finite Time Optimal Estimation* (CFTOE) problem to derive the optimal estimated values of switch side inductor current, $\hat{i}_{Lfs}$, capacitor voltage, $\hat{v}_{Cf}$, and grid side inductor current, $\hat{i}_{Lfo}$, with the samplings of capacitor voltage, v_{Cf}, and grid side inductor current, i_{Lfo}. The state-space equations for the discrete-time OBE can be expressed in standard matrix format of

$$\hat{X}_{k+1} = A_E\hat{X}_k + B_E u_k \tag{6a}$$

$$\hat{Y}_k = C_E\hat{X}_k + D_E u_k \tag{6b}$$

where the variables and matrices for OBE represent

$$A_E = \begin{bmatrix} 0 & -\frac{T_s}{L_{fs}} & 0 \\ \frac{T_s}{C_f} & 0 & -\frac{T_s}{C_f} \\ 0 & 0 & 0 \end{bmatrix}, B_E = \begin{bmatrix} \frac{T_s}{L_{fs}} \\ 0 \\ 0 \end{bmatrix}, \tag{7a}$$

$$C_E = \begin{bmatrix} 0 & 1 & 0 \\ 0 & 0 & 1 \end{bmatrix}, D_E = \begin{bmatrix} 0 \\ 0 \end{bmatrix}, \tag{7b}$$

$$\hat{X}_k = \begin{bmatrix} \hat{i}_{Lfs}(k) \\ \hat{v}_{Cf}(k) \\ \hat{i}_{Lfo}(k) \end{bmatrix}, \hat{Y}_k = \begin{bmatrix} \hat{v}_{Cf}(k) \\ \hat{i}_{Lfo}(k) \end{bmatrix}. \tag{7c}$$

Based on the OBE state-space equations in (6), the OBE solves for the optimal estimated state variable sequence of $\hat{X}_M, ..., \hat{X}_0$ with the known past measurement sampling sequence of $Y_M, ..., Y_0$ and input variable sequence of $u_M, ..., u_{-1}$. The cost function of OBE optimization problem is composed of two parts:
(1) Minimization of error between state equation (6a) and estimated state variable $\hat{X}_{j+1}$ which can be expressed as

$$e_{X,k} = (A_E\hat{X}_k + B_E u_k) - \hat{X}_{k+1}; \tag{8}$$

(2) Minimization of error between state equation (6b) and measured sampling output variable Y_j which can be expressed as

$$e_{Y,k} = (C_E\hat{X}_k + D_E u_k) - Y_k. \tag{9}$$

Thus, the OBE cost function for the CFTOE optimization can be expressed as

$$min \quad \sum_{k=M}^{-1} e_{X,k}^T Q_E e_{X,k} + \sum_{k=M}^{0} e_{Y,k}^T R_E e_{Y,k} \tag{10}$$

where Q_E and R_E represent the weighing factor matrices of the penalties that are implemented on the state variables and output variables, respectively.

The constraints of the OBE controller can be expressed as

$$e_{X,k} = (A_E\hat{X}_k + B_E u_k) - \hat{X}_{k+1} \in \mathcal{E}_{\mathcal{X}} \tag{11}$$

$$e_{Y,k} = (C_E\hat{X}_k + D_E u_k) - Y_k \in \mathcal{E}_{\mathcal{Y}} \tag{12}$$

$$\begin{bmatrix} -I_{Lfs,max} \\ 0 \\ -I_{Lfo,max} \end{bmatrix} \leq \hat{X}_k \leq \begin{bmatrix} I_{Lfs,max} \\ v_{in} \\ I_{Lfo,max} \end{bmatrix} \tag{13}$$

$$\begin{bmatrix} 0 \end{bmatrix} \leq u_k \leq \begin{bmatrix} v_{in} \end{bmatrix} \tag{14}$$

$$\begin{bmatrix} 0 \\ -I_{Lfo,max} \end{bmatrix} \leq Y_k \leq \begin{bmatrix} v_{in} \\ I_{Lfo,max} \end{bmatrix}. \tag{15}$$

For the purpose of reducing the OBE computation burden on a low cost DSP controller, the CFTOE optimization problem is solved explicitly by generating a piecewise affine function as is shown in Fig. 3(a). The specific implementing process of explicit OBE mechanism in Fig. 3(a) is demonstrated in Fig. 4. The state space equations of (6) and the constraints of the LC-based power module dynamic system are built offline to generate an online search tree and feedback law for OBE optimization. In each estimation implementing time period, the active region, r, is searched with the matrices $H_{r,E}$ and $K_{r,E}$. Then, in each of the specific active region, the corresponding feedback law matrices, $C_{r,E}$ and $D_{r,E}$, are applied to calculate the optimal output values, $\hat{Y}_k$, with the estimation horizon. Different colored regions in Fig. 3(a) represent various piecewise affine feedback law based on the measured variables.

For the real-time algorithm implementation, a binary search tree can find the optimal output values based on the updated state values of inductor current/output voltage [29]. Leveraging the Multi-Parametric Toolbox from [30], the explicit OBE avoids the time-consuming online optimization process, thus it is suitable for high frequency estimation. The binary search tree utilizes the theory in [29] by following a sequential search through the polyhedral regions of the partitions in Fig. 3 to find the optimal solution of the constrained optimization problem. For a clearer form of display, the colored areas of the generated piecewise affine region block with the state variables of i_{Lfs}, v_{Cf} and i_{Lfo} in Fig. 3(a) represent the m regions for OBE to search and optimize according to the feedback law.

B. Model Predictive Control

1) General Theory of MPC: For the general applications of MPC in power converters, (3) is applied for the theoretical model of the state-space system. The MPC algorithm is derived by solving the constrained finite time optimal control (CFTOC) problem. Thus, based on the general state space equations in (3), a cost function can be configured to minimize the tracking error between the state variable vector, $x(k)$, and the references, $\overline{x}(k)$, by predicting a series of future input variable, $u(k)$. The cost function can be generally expressed as:

This article has been accepted for publication in IEEE Transactions on Power Electronics. This is the author's version which has not been fully edited and content may change prior to final publication. Citation information: DOI 10.1109/TPEL.2022.3202863

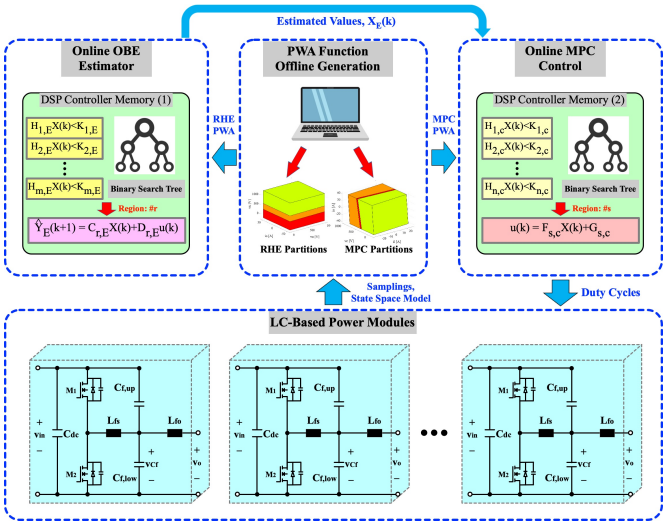

Fig. 4. The explicit implementation of OBE and MPC in DSP controller.

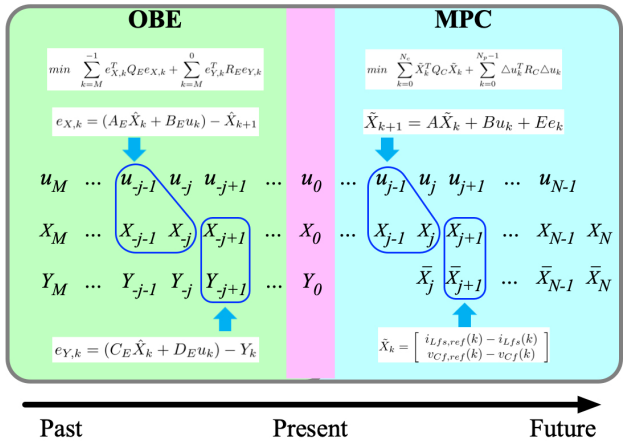

Fig. 5. Relationship between optimization-based estimation and model predictive control.

$$\underset{\substack{x(1),\ldots,x(N)\\ u(1),\ldots,u(N-1)}}{\operatorname{argmin}} \sum_{k=0}^{N-1} e_{x,k}^T \mathbf{Q}_C e_{x,k} + \sum_{k=0}^{N-1} e_{u,k}^T \mathbf{R}_C e_{m,k} + e_{u,N}^T \mathbf{P}_C e_{x,N}. \tag{16}$$

And the constraints are followed by:

$$s.t. \quad e_{x,k} = \overline{x}(k) - x(k) \tag{17a}$$
$$e_{u,k} = u(k) - u(k-1) \tag{17b}$$
$$x(k) \in \mathcal{X} \tag{17c}$$
$$u(k) \in \mathcal{U} \tag{17d}$$

where $k > 0$ in (16) and (17) means the information are expected for the prediction of the future instants. The weighing matrices, $\mathbf{Q}_C$ and $\mathbf{R}_C$, provide the penalties on the tracking errors and control input variations, respectively. The matrix, $\mathbf{P}_C$, is defined as the terminal cost which is a basic term in MPC that connects the properties between the finite time MPC and the infinite time LQR. The terminal cost is used to make sure of the stability, robustness and convergence.

2) Implementation of MPC for LC-Based Power Module: For the purpose of improving the dynamic performance, an explicit MPC method is designed for the per phase switch side capacitor voltage and inductor current control by solving the constrained finite time optimal control (CFTOC) problem. The switch side inductor currents are also regulated with the MPC by adjusting the weighing factor between i_{Lfs} and v_{Cf}. The benefits to configure the MPC (also OBE) for each of the LC-based power module instead of regarding multi-phase power modules as a whole circuitry application for the algorithm implementation can be concluded as: (1) the state space matrix of LC per phase is simple with lower order to implement the offline piecewise affine optimization code in a less costly DSP controller; (2) For AC interface applications, the time-varying angular speed term, ω, in dq reference frame can be omitted in the explicit MPC state space matrix for the offline optimization calculation; (3) Per phase MPC for LC is more flexible for a modular design perspective to extend the paralleled phase number and other topologies, e.g., DC/DC, single-phase DC/AC converters.

For the MPC implementation, in every control period, the MPC controller receives the measured switch side inductor current, i_{Lfs}, capacitor voltage, v_{Cf}, output side current, i_{Lfo}, from OBE of the optimal estimations and capacitor voltage reference, v_{Cf}^* from the cascaded controller or manual setup. An offline generated piecewise affine search tree is applied to derive the optimal duty cycle for the explicit MPC. The state equations of switch side LC filter can be expressed as

$$i_{Lfs}(k+1) = i_{Lfs}(k) - \frac{T_s}{L_{fs}} v_{Cf}(k) + \frac{v_{in} T_s}{L_{fs}} d(k) \tag{18a}$$
$$v_{Cf}(k+1) = \frac{T_s}{C_f} i_{Lfs}(k) + v_{Cf}(k) - \frac{T_s}{C_f} i_{Lfo}(k). \tag{18b}$$

For the flexibility of implementing the explicit MPC and the convenience of experimentally adjusting the DC bus voltage during test, the last term of (18), $v_{in}d(k)$, can be replaced by the phase leg output voltage, $v_x(k)$. The state-space model for MPC can be expressed in standard matrix format of

$$X_{k+1} = A_C X_k + B_C u_k + E_C e_k \tag{19}$$

where the variables and matrices for MPC control represent

$$A_C = \begin{bmatrix} 1 & -\frac{T_s}{L_{fs}} \\ \frac{T_s}{C_f} & 1 \end{bmatrix}, B_C = \begin{bmatrix} \frac{T_s}{L_{fs}} \\ 0 \end{bmatrix}, E_C = \begin{bmatrix} 0 \\ -\frac{T_s}{C_f} \end{bmatrix}, \tag{20a}$$

$$X_k = \begin{bmatrix} i_{Lfs}(k) \\ v_{Cf}(k) \end{bmatrix}, u_k = \begin{bmatrix} v_{in} d(k) \end{bmatrix}, e_k = \begin{bmatrix} i_{Lfo}(k) \end{bmatrix}. \tag{20b}$$

In the MPC formulation, the inductor current/capacitor voltage references can be defined as $\bar{X}$ and the tracking errors between the measurement and the references are expressed as $\tilde{X}$ which are composed of

$$\bar{X}_k = \begin{bmatrix} i_{Lfs,ref}(k) \\ v_{Cf,ref}(k) \end{bmatrix}, \tilde{X}_k = \begin{bmatrix} i_{Lfs,ref}(k) - i_{Lfs}(k) \\ v_{Cf,ref}(k) - v_{Cf}(k) \end{bmatrix}. \tag{21}$$

This article has been accepted for publication in IEEE Transactions on Power Electronics. This is the author's version which has not been fully edited and content may change prior to final publication. Citation information: DOI 10.1109/TPEL.2022.3202863

Thus, the cost function includes two terms

$$min \sum_{k=0}^{N_c} \tilde{X}_k^T Q_C \tilde{X}_k + \sum_{k=0}^{N_p-1} \triangle u_k^T R_C \triangle u_k. \quad (22)$$

For the penalties of the MPC cost function, Q_C and R_C represent the weighing factor matrices that are implemented on the state values and input values, respectively.

The constraints of the MPC controller can be expressed as

$$\tilde{X}_{k+1} = A\tilde{X}_k + Bu_k + Ee_k \in \mathcal{X} \quad (23)$$

$$\triangle u_k = u_k - u_{k-1} \in \mathcal{U} \quad (24)$$

$$\begin{bmatrix} -I_{Lfs,max} \\ 0 \end{bmatrix} \leq X_k \leq \begin{bmatrix} I_{Lfs,max} \\ v_{in} \end{bmatrix} \quad (25)$$

$$\begin{bmatrix} 0 \end{bmatrix} \leq u_k \leq \begin{bmatrix} v_{in} \end{bmatrix} \quad (26)$$

$$\begin{bmatrix} -I_{Lfo,max} \end{bmatrix} \leq e_k \leq \begin{bmatrix} I_{Lfo,max} \end{bmatrix}. \quad (27)$$

Similar with the OBE implemetation process, to achieve a high frequency control and reduce the computation load of the DSP, the MPC problem is also solved explicitly by generating a piecewise affine feedback law. Fig. 3(b) and Fig. 4 show the specific implementing process of explicit MPC mechanism. The state space model of (19) and constraints of the dynamic system are built offline to generate an online search tree and feedback law for MPC optimization. In each controlling time period, the active region, s, is searched with the matrices $H_{s,c}$ and $K_{s,c}$. Then, in each of the specific active region, the corresponding feedback law matrices, $F_{s,c}$ and $G_{s,c}$, are applied to calculate the optimal input values with the prediction horizon. Only the first value of the input sequence matrix is applied to the dynamic system for MPC control. Different colored regions in Fig. 3(b) represent various piecewise affine feedback low based on the estimated variables

In every control time period, a binary search tree can find the optimal duty cycle based on the updated state values of inductor current/output voltage. Explicit MPC avoids the time-consuming online optimization process, thus it is suitable for high frequency control. For a clearer form of display, the colored areas of the generated piecewise affine region block with the state variables of i_{Lfs}, v_{Cf} and i_{Lfo} in Fig. 3(b) represent the n regions for MPC to search and optimize according to the feedback law. Specifically, the matrices $H_{s,c}$ and $K_{s,c}$ will lead to an active region. The corresponding matrices $F_{s,c}$ and $G_{s,c}$ will help calculate the optimal duty cycle for the PWM signals.

The working mechanisms of OBE and MPC are symmetrical with respect to the present state. Specifically, OBE is dealing with the states from past to present steps and MPC is optimizing the states from present to the future steps. The relationship between OBE and MPC has been shown in Fig. 5.

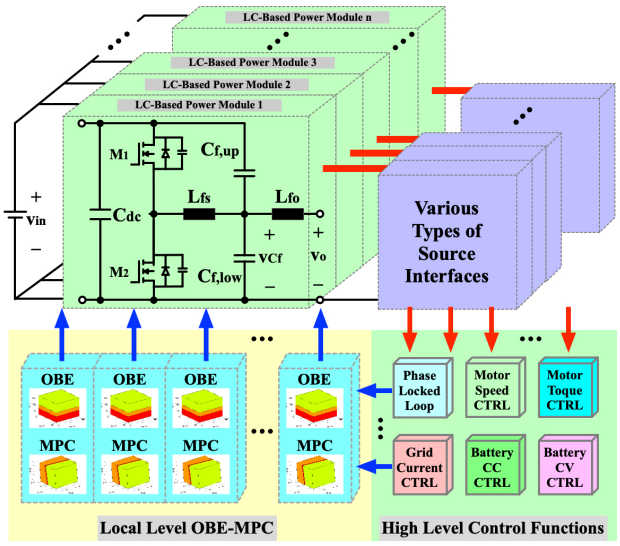

Fig. 6. The software-defined OBE-MPC power module-based power electronics architecture interfaced with wide applications.

IV. OBE-MPC for DC/DC, DC/AC Grid and Motor Applications

With the basic LC power module in Fig. 1, the proposed integrated OBE-MPC technique can be applied to each of the power unit as is shown in Fig. 2 to build the software-defined powr electronics architecture and enable a wide range of applications. Thus, different number of the power modules combined with the OBE-MPC algorithms can be reconfigured in Fig. 6 as desired circuitry topologies for various application purposes, e.g., single/three-phase DC/AC inverters, motor traction inverter, multi-phase DC/DC converters to reduce the sensor cost, sampling noise and improve the dynamic performance. As is shown in Fig. 6, the software-defined OBE-MPC power module-based power electronics architecture is composed of high level control functions and local level OBE-MPC function. The high level control functions mainly include the holistic control algorithms for different applications. The local level OBE-MPC function is the algorithms designed in this paper for each of the LC-based power module.

A. DC/DC Application

The first application for the developed OBE-MPC technique is DC/DC interfaced power converter as is shown in Fig. 7. The combined OBE-MPC algorithms are configured in the LC-based power module to control the output voltage, v_o. Specifically, the output capacitor voltage, v_{Cf}, and output current, i_o, are directly measured as the output variable matrix, Y_k, in (6). The inductor current, $\hat{i_L}$, output capacitor voltage, $\hat{v_{Cf}}$, and output current, $\hat{i_o}$, are configured as the estimated state variable matrix, $\hat{X_k}$. Based on the OBE cost function in (10) and the corresponding constraints in (11)-(15) to deal with the past sampling information within the estimation horizon, the optimal estimation of $\hat{X_k}$ will be derived for the purpose of MPC control process with less noise.

Symmetrically with OBE, the MPC manages the future sampling information within the prediction horizon to derive the

This article has been accepted for publication in IEEE Transactions on Power Electronics. This is the author's version which has not been fully edited and content may change prior to final publication. Citation information: DOI 10.1109/TPEL.2022.3202863

optimal input variable matrix, u_k, of duty cycle by solving the MPC cost function in (22) and the corresponding constraints in (23)-(27). Instead of using the noisy sampling state variables of X_k, the MPC utilizes the estimated state variables, $\hat{X}_k$, from OBE to track the output capacitor voltage reference with less noise and oscillation.

B. DC/AC Application

The second application for the developed OBE-MPC is DC/AC interfaced power converters. As are shown in Fig. 8 and 9, the OBE-MPC equipped LC-based power modules can be reconfigured as single/three-phase grid-connected inverters with two/three power modules, respectively.

1) Single-phase grid: For the DC/AC single-phase inverter and the corresponding control diagram in Fig. 8, the OBE-MPC algorithms are configured for each of the two LC-based power modules. Similarly with the DC/DC control diagram of Fig. 7, the OBE derives the estimation of three variables, inductor current, $\hat{i_L}$, output capacitor voltage, $v_{\hat{Cf}}$, and grid current, $\hat{i_g}$, for MPC control process to achieve less noise, reduced sensor count and improved dynamic performance. The outer loop grid current control is implemented in $dq0$ reference frame with PI controllers to track the specific d and q components of the single-phase grid current, $i^*_{g,d}$ and $i^*_{g,q}$, respectively. Then the outer loop grid current controller exports the d and q components of the output capacitor voltage references, $v^*_{Cf,d}$ and $v^*_{Cf,q}$, for the inner loop per phase power module OBE-MPC implementation. Since the inner loop OBE-MPC algorithm is implemented in ab reference frame for each phase, the Park/Clarke transformations are inserted between the outer and inner loops to convert and allocate the output capacitor voltage references from $dq0$ to ab frame as $v^*_{Cf,a}$ and $v^*_{Cf,b}$ for the two phases of single-phase inverter application. In addition to the dq components, the zero-sequence control branch is also configured to control the zero-sequence capacitor voltage as half of DC bus voltage, $v_{dc}/2$, to stabilize the common mode voltage and attenuate the leakage current from flowing into the single-phase grid in the non-isolated circuit topology.

2) Three-phase grid: For the DC/AC three-phase inverter and the corresponding OBE-MPC control diagram in Fig. 9, the control principle is similar with the single-phase inverter application. Instead of two LC-based power modules, three power modules with the corresponding OBE-MPC algorithms are constructed to be interfaced with a three-phase grid for higher power capability. The outer loop grid current control is also implemented in $dq0$ reference frame with PI controllers to track the specific d and q components of the three-phase grid current, $i^*_{g,d}$ and $i^*_{g,q}$, respectively. Then the outer loop grid current controller exports the d and q components of the output capacitor voltage references, $v^*_{Cf,d}$ and $v^*_{Cf,q}$, for the inner loop per phase power module OBE-MPC implementation. Since the inner loop OBE-MPC algorithm is implemented in abc reference frame for each phase, the Park/Clarke transformations are inserted between the outer and inner loops to convert and allocate the output capacitor voltage references from $dq0$ to abc frame as $v^*_{Cf,a}$, $v^*_{Cf,b}$ and $v^*_{Cf,c}$ for the three phases of three-phase inverter application. In addition to the dq components, the zero-sequence control branch is also configured to control the zero-sequence capacitor voltage as half of DC bus voltage, $v_{dc}/2$, to stabilize the common mode voltage and attenuate the leakage current from flowing into the three-phase grid in the non-isolated circuit topology.

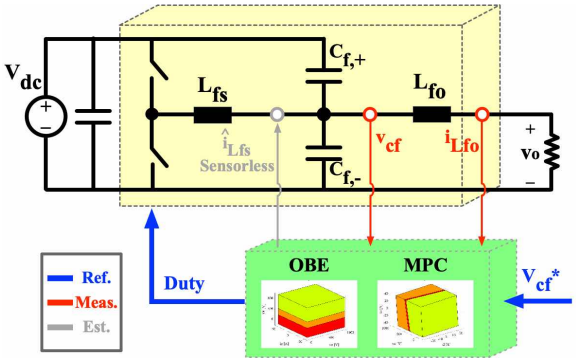

Fig. 7. The integrated OBE and MPC control diagram for the DC/DC interfaced application with LC-based power module.

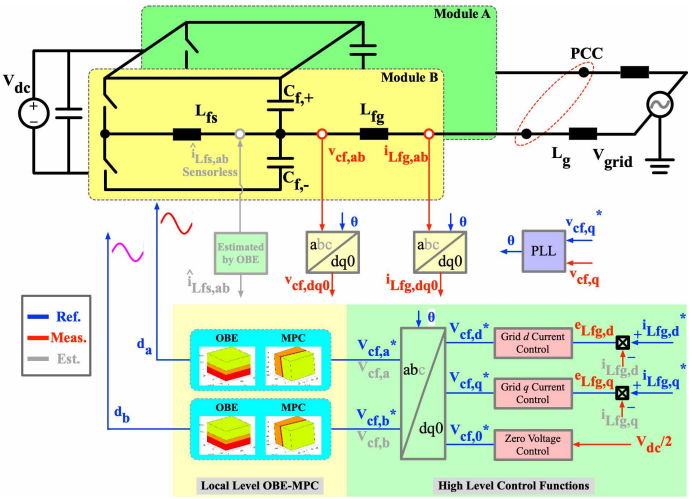

Fig. 8. The integrated OBE and MPC control diagram for the DC/AC single-phase interfaced application with LC-based power modules.

To conclude for both of the single/three-phase DC/AC grid applications, the OBE contributes to the noise attenuation from the sampling ADC data and cost reduction on sensor count. The MPC improves the dynamic performance with higher tracking speed and less oscillation due to the increased control bandwidth enabled by the inner loop MPC. Also, the developed cascaded control architecture does not leverage the grid side inductor for MPC parametric modeling. This strategy avoids the unexpected MPC modeling parametric error from the interfaced grid caused by the unknown grid side equivalent inductance. Thus, the accuracy is further improved.

C. Motor Application

The third application for the developed OBE-MPC is motor drive. As are shown in Fig. 10, three of the OBE-MPC equipped LC-based power modules can be configured as motor traction inverter. The control diagram can be divided

This article has been accepted for publication in IEEE Transactions on Power Electronics. This is the author's version which has not been fully edited and content may change prior to final publication. Citation information: DOI 10.1109/TPEL.2022.3202863

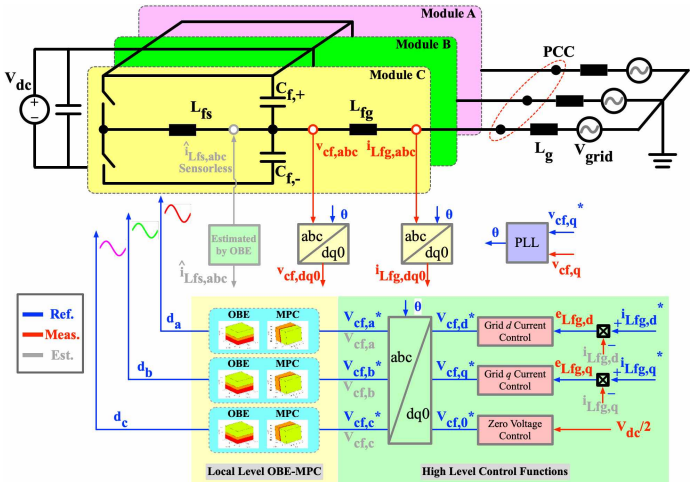

Fig. 9. The integrated OBE and MPC control diagram for the DC/AC three-phase interfaced application with LC-based power modules.

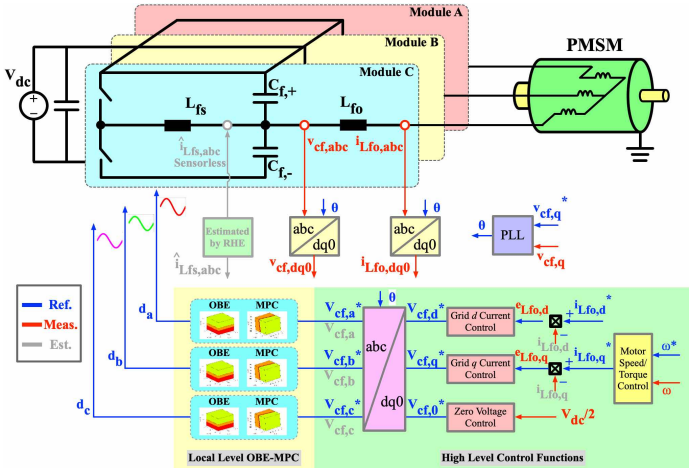

Fig. 10. The integrated OBE and MPC control diagram for the DC/AC motor interfaced application with LC-based power modules.

into three cascaded loops: outer loop motor speed control, middle loop motor current control and inner loop OBE-MPC control. The outer loop speed controller is cascaded on top of the middle loop motor current q component controller to regulate the motor speed, ω with the desired reference, ω^*. Then the middle loop motor current controller exports the d and q components of the output capacitor voltage references, $v^*_{Cf,d}$ and $v^*_{Cf,q}$, for the inner loop per phase power module OBE-MPC implementation. Since the inner loop OBE-MPC algorithm is also implemented in abc reference frame for each phase, the Park/Clarke transformations are inserted between the middle and inner loops to convert and allocate the output capacitor voltage references from $dq0$ to abc frame as $v^*_{Cf,a}$, $v^*_{Cf,b}$ and $v^*_{Cf,c}$ for the three phases of motor application. In addition to the dq components, the zero-sequence control branch is also configured for the motor traction inverter to control the zero-sequence capacitor voltage as half of DC bus voltage, $v_{dc}/2$, to stabilize the shaft voltage and attenuate the bearing current. With the zero-sequence stabilization, the possibility of motor failure can be reduced accordingly with less oscillation on shaft voltage and bearing current.

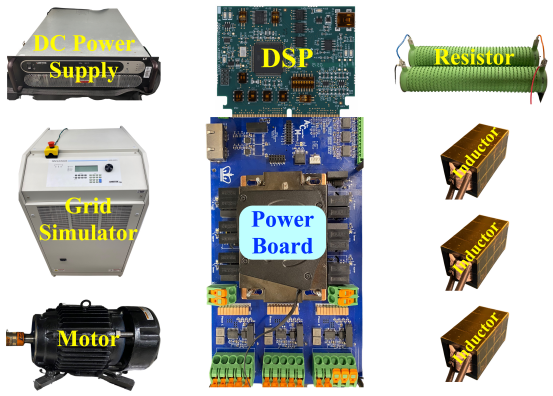

Fig. 11. The test bench for the implementation of OBE-MPC algorithms.

The studied topologies for the applications of DC/DC, DC/AC and motor interfaces are equivalent to the general ones to implement the proposed OBE-MPC algorithms. The upper and lower output capacitors in Fig. 1 are functioned as the LC filtering for output current and voltage. The equivalent capacitance for output filtering is same as the conventional topology by adding the upper/lower capacitance together. Thus, even though the number of capacitors are doubled, the total capacitance utilization is not sacrificed.

V. Merits and Validation

The OBE-MPC algorithms for the LC-based power modules are validated experimentally in this section for various applications, e.g., DC/DC converter, single/three-phase grid-connected inverters. The test bench is shown in Fig. 11 including the power board, control card, inductors, AC grid simulator, DC powr supply and resistor. The power switches are C3M0032120K SiC MOSFETs from CREE. The DSP controller is F280049C controlCARD from TI.

The merits of the developed OBE-MPC can be concluded in four aspects: (1) less sensor count by OBE for low cost; (2) lower noise by OBE for more stable control performance; (3) better dynamic performance by MPC for more robust transient; (4) less computation burden by explicit implementation of OBE-MPC on a low cost DSP; (5) wide applications with the OBE-MPC algorithms on the generalized LC-based power module; (6) accurate state space parametric modeling of OBE-MPC for LC-based power module without the influence of uncertainty and error from the output side interfaced unknown inductance. The switching frequency and sampling frequency are both configured as 80kHz. The control frequency is set as 20kHz. In each control period, the sampled state variables are averaged with a factor of 4 to filter out the circuitry noise for better control performance.

A. Steady State Performance of OBE-MPC

The steady state performance of OBE-MPC is demonstrated in this section to show the noise/oscillation reduction and estimation accuracy of OBE and the tracking accuracy of MPC. Specifically, Fig. 12 shows the output current, capacitor

This article has been accepted for publication in IEEE Transactions on Power Electronics. This is the author's version which has not been fully edited and content may change prior to final publication. Citation information: DOI 10.1109/TPEL.2022.3202863

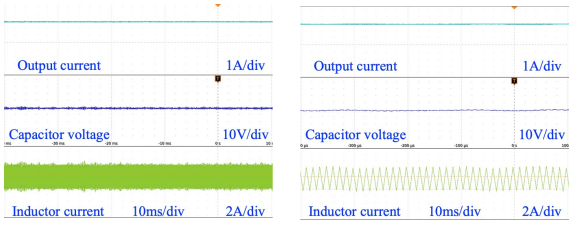

Fig. 12. OBE-MPC (a) experimental and (b) zoomed waveforms of output current, capacitor voltage, inductor current for DC/DC converter.

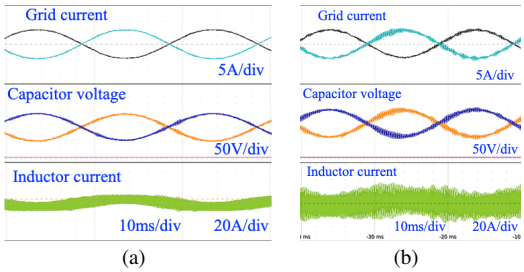

Fig. 13. Experimental waveforms of grid-interfaced single-phase DC/AC inductor current, capacitor voltage, grid current and DC bus voltage for MPC control (a) combined with OBE and (b) without OBE.

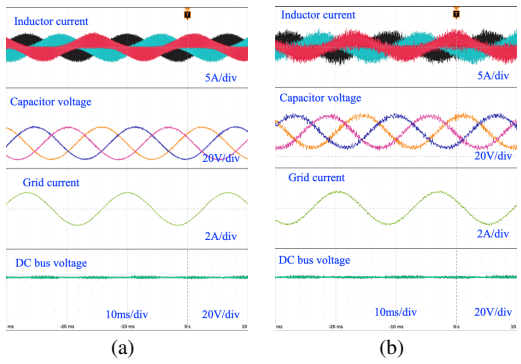

Fig. 14. Experimental waveforms of grid-interfaced three-phase DC/AC inductor current, capacitor voltage, grid current and DC bus voltage for MPC control (a) combined with OBE and (b) without OBE.

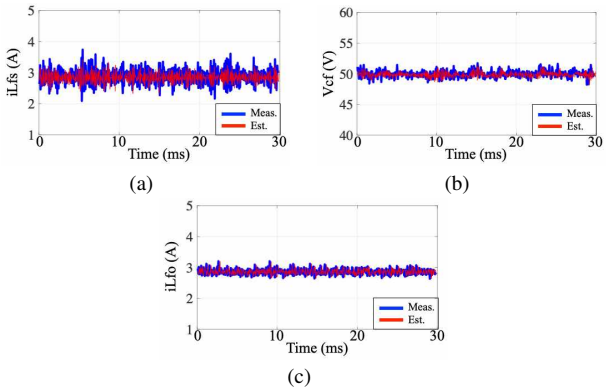

Fig. 15. OBE estimation performance of the experimentally captured steady state ADC readings of measurement and estimation for DC/DC application (a) inductor current (b) capacitor voltage and (c) output current.

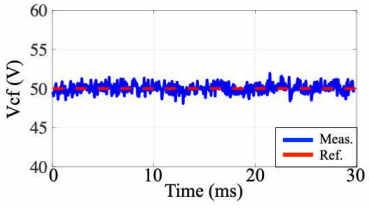

Fig. 16. MPC tracking performance of the experimentally captured steady state ADC readings of capacitor voltage for the DC/DC application.

voltage and inductor current waveforms of the DC/DC converter with OBE-MPC method. Fig. 13(a) and 13(b) compare the grid current, output capacitor voltage and inductor current of single-phase grid-interfaced DC/AC converter with and without OBE, respectively. Also, Fig. 14(a) and 14(b) show the comparison with and without OBE for the three-phase grid DC/AC inverter, respectively. Both of the grid-connected applications demonstrate that OBE can reduce the noise and oscillation.

Furthermore, for the DC/DC application, the experimentally captured ADC readings of measurement and estimation for inductor current, capacitor voltage and output current are shown in Fig. 15. Fig. 16 shows the MPC reference and measurement for DC/DC converter output capacitor voltage where the MPC accurately tracks a voltage reference of 50V. For the grid interfaced application, the experimentally captured ADC readings of measurement and estimation for inductor current, capacitor voltage and grid current are shown in Fig. 17. The sampling noise from sensor is largely reduced by OBE for a more stable performance. And the estimation accuracy is high with a relatively low estimation error as is shown in Fig. 18. Fig. 19(a) and 19(b) show the MPC references and measurement for grid q current and output capacitor voltage which demonstrate the high tracking accuracy of MPC.

For the influence of parasitic circuit on the control accuracy, the pre-designed parasitic resistor and capacitor, R_{para} and C_{para}, are manually connected between the DC bus terminal and neutral point of grid simulator. The values of the R_{para} and C_{para} are selected based on the typical parasitic range between the automotive and photovoltaic systems. The corresponding control accuracy with different values of R_{para} and C_{para} has been shown in Table I. It can be demonstrated that the parasitic values has limited influence on the control accuracy.

B. Transient Performance of OBE-MPC

The transient performance of OBE-MPC is demonstrated in this section to show the noise/oscillation reduction and estimation accuracy of OBE and the tracking accuracy and dynamic performance of MPC. Specifically, Fig. 20(a) and 20(b) show the single- and three-phase grid-interfaced inverters grid current, output capacitor voltage and inductor current transient waveforms with current steps from 8A to 2A and 2A to 10A, respectively. For the application of DC/DC converter, Fig. 21 captures the experimental ADC readings of measurement and estimation for inductor current, output capacitor voltage and output current with a voltage step from 20V to 50V.

This article has been accepted for publication in IEEE Transactions on Power Electronics. This is the author's version which has not been fully edited and content may change prior to final publication. Citation information: DOI 10.1109/TPEL.2022.3202863

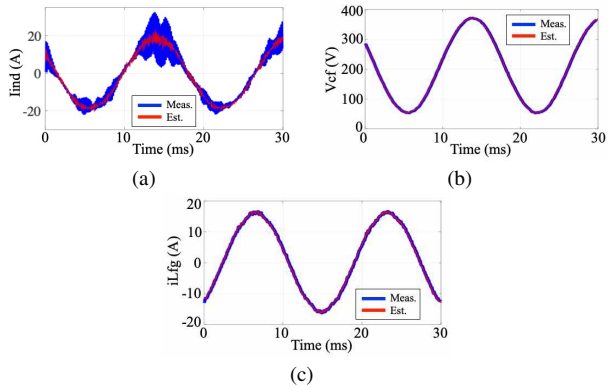

Fig. 17. OBE estimation performance of the experimentally captured steady state ADC readings of measurement and estimation for grid-interfaced (a) inductor current (b) capacitor voltage and (c) grid current.

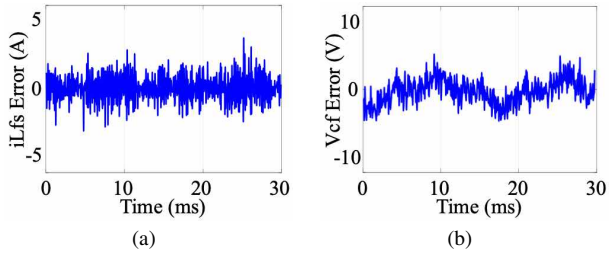

Fig. 18. OBE performance of the experimentally captured ADC readings of the estimation errors for grid-interfaced (a) inductor current and (b) capacitor voltage.

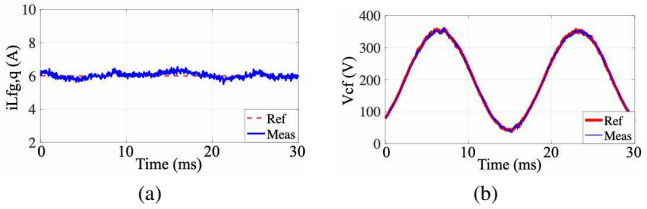

Fig. 19. MPC tracking performance of the experimentally captured steady state ADC readings of measurement and reference for grid-interfaced (a) grid q current at 6A and (b) capacitor voltage.

The OBE can accurately estimate the measurements with less noise/oscillation especially during the transient. Fig. 22 performs the experimental ADC readings of capacitor voltage measurement and the corresponding MPC reference with a step of 30V. The MPC tracks the reference steadily within 2ms. Furthermore, Fig. 23 captures the experimental ADC readings of measurement and estimation for grid-interfaced inverter inductor current, output capacitor voltage and grid current with a current step from 0A to 10A. The OBE can accurately estimate the measurements with less noise/oscillation during the transient. Fig. 24 demonstrates the motor drive application of the OBE-MPC with a speed step from 260 rpm to -260 rpm in Fig. 24(a) and a torque step from -5 Nm to 5 Nm in Fig. 24(b), respectively. Also, the measured and estimated dq components of the switch side inductor currents and the corresponding erorrs for motor application have been shown in Fig. 25.

C. Robustness and Stability of Control

The robustness and stability of the control performance are demonstrated in this subsection. For the proposed multi-level control method, the corresponding control and system plant model has been shown in Fig. 26. The local level per phase switch side LC MPC is cascaded with the high level of grid side inductor current control. A linear-quadratic regulator (LQR) can be applied to derive the transfer function for the MPC algorithm portion in the control plant model of Fig. 26 to solve the cost function.

The typical LQR control diagram integrated with a dynamic system is shown in the bottom block of Fig. 26 where x, y, u, r represent the state variable, $[i_{Lfs}; v_{Cf}]$, output variable, i_{Lfs}, input variable of duty cycle, d, and tracking reference, $i_{Lfs,ref}$, respectively. The core algorithm of MPC to calculate the optimal duty cycle is a linear coefficient matrix, -**K**. And the MPC equation to calculate the optimal duty cycle based on the tracking error and state variable can be expressed as:

$$d = -\mathbf{K}\begin{bmatrix} i_{Lfs} \\ v_{Cf} \\ v_{Cf,err} \end{bmatrix} = -[K_{11}, K_{12}, K_{13}]\begin{bmatrix} i_{Lfs} \\ v_{Cf} \\ v_{Cf,err} \end{bmatrix} \tag{28}$$

where $v_{Cf,err}$ is the tracking error of the MPC calculated as $v_{Cf,ref} - v_{Cf}$.

Thus, the local level MPC can be expressed in the transfer function as Fig. 26. The transfer function from tracking error, $v_{Cf,err}$, to the measurement, v_{Cf}, of output capacitor voltage can be expressed as:

$$\begin{aligned} &G_{vCferr2vCf,MPC}(s) = \\ &\frac{-K_{13}G_{LCL,vx2ig}(s)(sL_{fg}+R_{Lfg})(sL_{fs}+R_{Lfs})/V_{dc}}{\{(sL_{fs}+R_{Lfs})+K_{11}[V_{dc}-G_{LCL,vx2ig}(s)(sL_{fg}+R_{Lfg})]/V_{dc}+} \\ &K_{12}G_{LCL,vx2ig}(s)(sL_{fs}+R_{Lfs})(sL_{fg}+R_{Lfg})/V_{dc}- \\ &K_{13}G_{LCL,vx2ig}(s)(sL_{fs}+R_{Lfs})(sL_{fg}+R_{Lfg})/V_{dc}\}. \end{aligned} \tag{29}$$

Furthermore, the transfer function from the reference, $v_{Cf,ref}$, to the measurement, v_{Cf}, of output capacitor voltage can be expressed as:

$$\begin{aligned} &G_{vCfref2vCf,MPC}(s) = \\ &G_{vCferr2vCf,MPC}(s)/[1+G_{vCferr2vCf,MPC}(s)]. \end{aligned} \tag{30}$$

Based on equation (30) and the LCL plant model in Fig. 26, the transfer function from the reference of output capacitor voltage, $v_{Cf,ref}$, to the measurement of grid side inductor current, i_{Lfg}, can be derived as:

$$\begin{aligned} &G_{vCfref2iLfg,MPC}(s) = \\ &G_{vCfref2vCf,MPC}(s)/(sL_{fg}+R_{Lfg}). \end{aligned} \tag{31}$$

Then, taking the high level grid side inductor current PI control into consideration, the cascaded MPC transfer function from tracking error, $i_{Lfg,err}$, to the measurement, i_{Lfg}, of grid side inductor current can be expressed as:

$$\begin{aligned} &G_{iLfgerr2iLfg,MPC}(s) = \\ &G_{vCfref2iLfg,MPC}(s)\cdot G_{iLfg,PI}(s). \end{aligned} \tag{32}$$

This article has been accepted for publication in IEEE Transactions on Power Electronics. This is the author's version which has not been fully edited and content may change prior to final publication. Citation information: DOI 10.1109/TPEL.2022.3202863

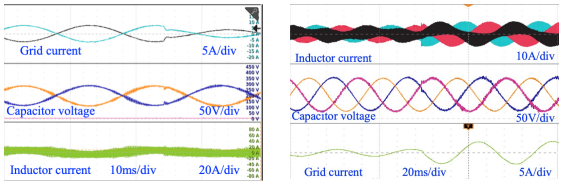

Fig. 20. Transient performance of the experimental inductor current, output capacitor voltage and grid current waveforms for grid-interfaced applications of (a) single-phase DC/AC inverter with grid current step from 8A to 4A and (b) three-phase DC/AC inverter with grid current step from 4A to 10A.

The cascaded MPC transfer function from tracking error of grid side inductor, $i_{Lfg,err}$, to the measurement of output capacitor voltage, v_{Cf}, can be expressed as:

$$G_{iLfgerr2vCf,MPC}(s) = G_{vCfref2vCf,MPC}(s) \cdot G_{iLfg,PI}(s). \quad (33)$$

The resonance behavior and dynamic performance of the three control strategies for LCL filtered grid-connected inverter are analyzed based on the derived transfer functions. Fig. 27(a) and Fig. 27(b) show the bode plots comparison of transfer functions from the tracking error to the measurement of grid side inductor current and from the tracking error of grid side inductor current to the measurement of output capacitor voltage, respectively. The magnitude plots demonstrate that the conventional PI control has a convex spike at the resonant frequency point. The notch filtered PI control has a concave spike at the resonant frequency point. The developed cascaded MPC attenuates the spike at the resonant frequency point and the control bandwidth is wider than the conventional PI, notch filtered PI and cascaded PI methods. The robustness and stability are improved correspondingly. For the dynamic performance comparison of PI control, notch filtered PI control and cascaded MPC methods, Fig. 28 shows the $i_{Lfg,q}$ steps and zoomed waveforms from 2A to 8A under four testing cases: (1) PI control with K_p gain of 20; (2) notch filtered PI control with K_p gain of 20; (3) PI control with K_p gain of 2; (4) cascaded MPC control with K_p gain of 20. It can be seen that the the proposed cascaded MPC behaves more stable than either PI control or notch filtered PI control at high K_p gain of 20 with less overshoot and oscillation. Even though the PI method can act stably with a smaller K_p gain of 2, the response time is much longer than the proposed cascaded MPC method. Thus, the robustness and stability are improved with the cascaded MPC.

TABLE I
INFLUENCES OF PARASITIC VALUES ON TRACKING ACCURACY

R_{para} [Ω]	C_{para} [nF]	Tracking Error
40	400	0.75%
30	300	0.55%
20	200	0.64%
10	100	0.83%
5	50	0.79%

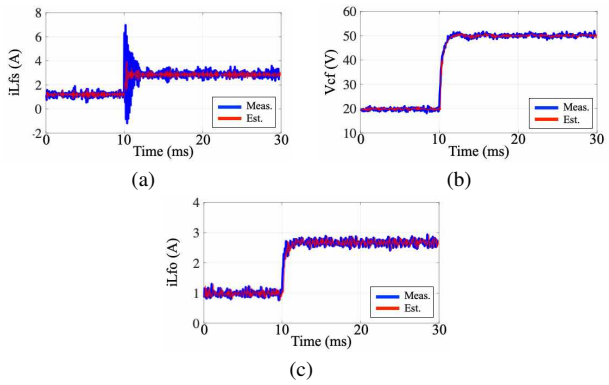

Fig. 21. OBE estimation performance of the experimentally captured transient ADC readings of measurement and estimation with a voltage step from 20V to 50V for DC/DC application (a) inductor current (b) capacitor voltage and (c) output current.

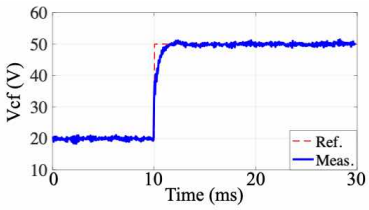

Fig. 22. MPC tracking performance of the experimentally captured transient ADC readings of capacitor voltage with a step from 20V to 50V for the DC/DC application.

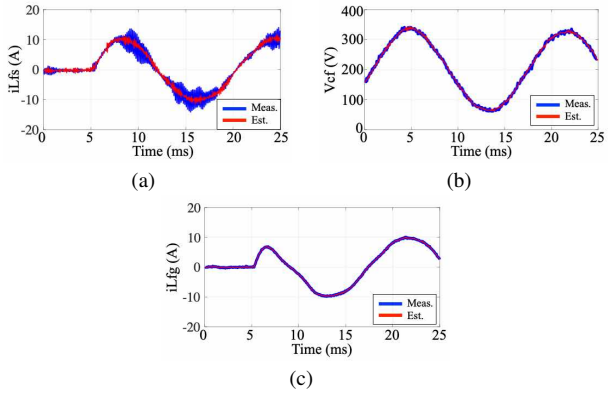

Fig. 23. OBE estimation performance of the experimentally captured transient ADC readings of measurement and estimation with a current step of 10A for grid-interfaced (a) inductor current (b) capacitor voltage and (c) grid current.

D. Comparison of OBE-MPC with Conventional Methods

The comparison between the proposed OBE-MPC with conventional estimation and control methods are analyzed in this subsection.

1) Control comparison: For the control comparison with the conventional MPC methods, three aspects are demonstrated including computation burden, parametric accuracy and control performance. Firstly, for the computation complexity, in the LCL filter inverter system, the conventional MPC methods typically require high order state space equations. The state space matrix, $\mathbf{A}$, is 9×9 in [31], 4×4 in [32] and 3×3 in [33], [34]. However, in the proposed MPC method, since only

This article has been accepted for publication in IEEE Transactions on Power Electronics. This is the author's version which has not been fully edited and content may change prior to final publication. Citation information: DOI 10.1109/TPEL.2022.3202863

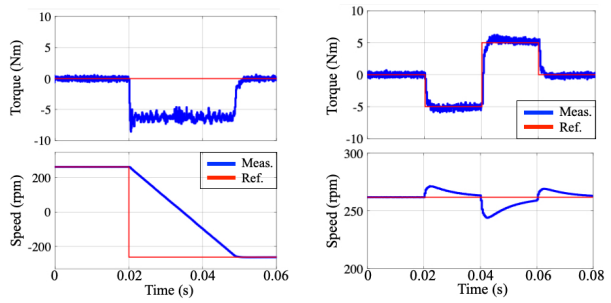

Fig. 24. OBE-MPC for motor drive application with (a) a speed step from 260 rpm to -260 rpm and (b) a torque step from -5 Nm to 5 Nm.

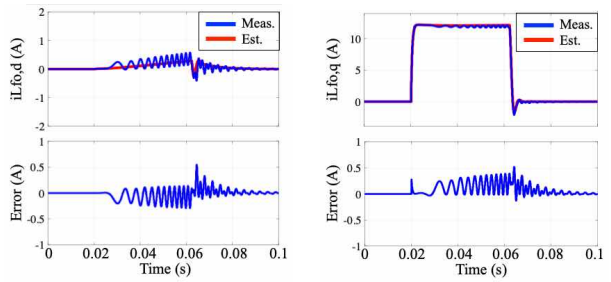

Fig. 25. OBE-MPC comparison between estimation and measurement and the corresponding estimation error for motor drive application of (a) $i_{Lfo,d}$ and (b) $i_{Lfo,q}$ currents with speed step transient.

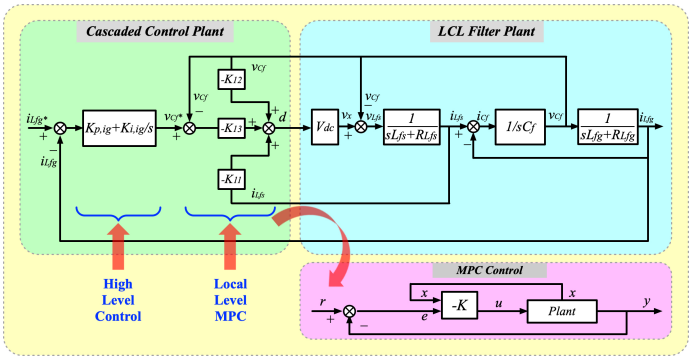

Fig. 26. The holistic diagram of cascaded MPC control and plant model.

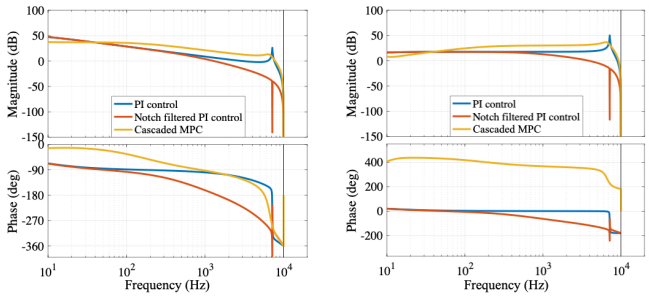

Fig. 27. Comparison of bode plots for the control strategies of conventional PI, notch filtered PI and the proposed MPC (a) from $i_{Lfg,err}$ to i_{Lfg} and (b) from $i_{Lfg,err}$ to v_{Cf}.

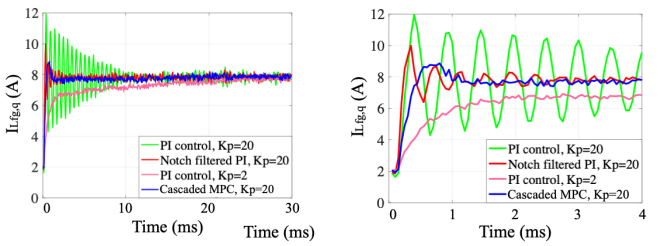

Fig. 28. Comparison of PI, notch filtered PI and MMPC transient captured ADC readings of (a) grid side inductor current q component from 2A to 8A and (b) zoomed waveforms.

switch side LC filter parameters are necessary for the state space formulation, the matrix order is reduced to be 2×2 in (20a). Thus, the online computation burden is reduced accordingly. The generated C code for the developed MPC algorithm is 5KB which is 2-3 times smaller than the third and fourth order state space matrices systems. The execution time on the TI F280049C controlCARD is 4μs which is 2 times faster than the third order state space matrices systems. Secondly, for the parametric accuracy, since the developed control method is two-level multi-layer architecture, the equivalent inductance and resistance from the output side interfaced applications will not influence the MPC parametric modeling of the LC-based power module. Thus, the accuracy of the MPC can be guaranteed without being affected by the uncertainty of the interfaced output inductance. However, for the conventional MPC methods with LCL converters in [31]–[34], both the switch side and output side inductance values are required for the parametric modeling which may result in error caused by the unknown output impedance. Thirdly, for the control performance, the proposed method achieves the overshoot, rise/fall time and practical bandwidth ($0.35/T_{rise}$) of $\leq$10%, $\leq$1ms and $\geq$800Hz. The overshoot, rise/fall time and practical bandwidth in the conventional methods are 20%, 4ms, 100Hz for [35], 5%, 5ms, 80Hz for [36] and 3%, 20ms, 20Hz for [37].

2) Estimation comparison: For the estimation comparison with the conventional methods, four aspects are demonstrated including noise reduction, estimation error, parametric accuracy and sensor count. Firstly, for the noise reduction, the extended state observer estimation method in [38] requires a digital filter to attenuate the noise from the measured and estimated values. A reduced order generalized parameter estimation-based observer is presented in [39] for the estimation of state variables. The system noise can be attenuated by increasing the filter gain, λ, but the transient performance will be sacrificed. The disturbance-based estimation method reported in [40] is shown to be affected by Gaussian random noise on the output voltage side. The developed OBE reduces the noise by 60% and 25% on the switch side inductor current and output capacitor voltage which demonstrates the noise reduction capability. Thirdly, for the parametric accuracy, similarly to the MPC modeling, since the OBE is configured in each of the local level power module of the multi-layer control/estimation

structure, the equivalent inductance and resistance from the output side interfaced applications will not influence the OBE parametric modeling of the LC-based power module. Thus, the accuracy of the OBE can be guaranteed without being affected by the uncertainty of the interfaced output inductance. However, the conventional estimation methods for the application of LCL filtered converters require the unknown output side inductance which may result in error caused by the unknown output impedance [38], [39]. Lastly, for the sensor count, the conventional control methods in [31]–[34] require all the switch side current, output capacitor voltage and output side current sensors to achieve the targets. The conventional estimation algorithm in [38] is based on the measurement of switch side inductor current value in single-phase LCL filter inverter with one current sensor. [41], [42] utilize the grid voltage and switch side inductor current sensors to estimate the output voltage for control. [43] leverages either the switch or grid side inductor current sensor along with the grid voltage sensor to perform active damping for LCL converter. [44] has designed the disturbance observer with the measurements of grid side inductor current and grid voltage sensors to estimate the switch side inductor current and output capacitor voltage values. The proposed OBE-MPC for each power module uses output side inductor current and output capacitor voltage sensors to optimally estimate the switch side inductor current, output capacitor voltage and output side inductor current for control purpose.

The comparison among OBE, MPC and the conventional PI control in noise reduction, estimation/tracking error, rise time, C code size and execution time has been summarized in Table II to shown the merits of the designed algorithms.

VI. Conclusion

This paper develops a combined OBE-MPC technique for the software-defined LC power module-based power electronics architecture that can be leveraged for wide applications, e.g., DC/DC converters, single/three-phase DC/AC grid-connected inverters and motor traction inverter. With the OBE, the sensor count is reduced with lower cost and the sampling noise is attenuated with more stable control performance. With the MPC, the dynamic performance is improved with faster tracking speed and more robust transient. The explicit implementation of OBE-MPC relieves the computation burden and enables the application on low cost DSP. Different number of the OBE-MPC LC-based power modules are reconfigured to satisfy various load/source requirements and achieve highly accurate parametric modeling without being influenced by the unknown output inductance. The experiments have validated the developed algorithms and control architectures.

TABLE II
Merits Summary of OBE and MPC

	Inductor current, I_{ind}	Capacitor voltage, V_{cap}
OBE noise reduction	60%	25%
OBE estimation error	3.2%	1.3%
MPC tracking error	2.4%	1.1%
MPC rise time.	1.5ms	2ms
Conventional PI rise time	15ms	23ms
	File size	Execution time
Generated OBE C code	10KB	7.12μs
Generated MPC C code	5KB	4.04μs
Conventional PI C code	1KB	1.04μs

References

[1] A. Moulichon, M. Alamir, V. Debusschere, L. Garbuio, M. A. Rahmani, M.-X. Wang, and N. Hadjsaid, "Observer-based current controller for virtual synchronous generator in presence of unknown and unpredictable loads," *IEEE Transactions on Power Electronics*, vol. 36, no. 2, pp. 1708–1716, 2021.

[2] Z. Dai, W. Lin, and H. Lin, "Estimation of single-phase grid voltage parameters with zero steady-state error," *IEEE Transactions on Power Electronics*, vol. 31, no. 5, pp. 3867–3879, 2016.

[3] S. Zhu, W. Huang, Y. Zhao, X. Lin, D. Dong, W. Jiang, Y. Zhao, and X. Wu, "Robust speed control of electrical drives with reduced ripple using adaptive switching high-order extended state observer," *IEEE Transactions on Power Electronics*, vol. 37, no. 2, pp. 2009–2020, 2022.

[4] T. V. Tran, K.-H. Kim, and J.-S. Lai, "Optimized active disturbance rejection control with resonant extended state observer for grid voltage sensorless lcl-filtered inverter," *IEEE Transactions on Power Electronics*, vol. 36, no. 11, pp. 13 317–13 331, 2021.

[5] Z. Yin, C. Bai, N. Du, C. Du, and J. Liu, "Research on internal model control of induction motors based on luenberger disturbance observer," *IEEE Transactions on Power Electronics*, vol. 36, no. 7, pp. 8155–8170, 2021.

[6] Q. Ouyang, J. Chen, and J. Zheng, "State-of-charge observer design for batteries with online model parameter identification: A robust approach," *IEEE Transactions on Power Electronics*, vol. 35, no. 6, pp. 5820–5831, 2020.

[7] A. Alessandri, M. Baglietto, and G. Battistelli, "Receding-horizon estimation for switching discrete-time linear systems," *IEEE Transactions on Automatic Control*, vol. 50, no. 11, pp. 1736–1748, 2005.

[8] K. Ling and K. Lim, "Receding horizon recursive state estimation," *IEEE Transactions on Automatic Control*, vol. 44, no. 9, pp. 1750–1753, 1999.

[9] W. Xu, R. Dian, Y. Liu, D. Hu, and J. Zhu, "Robust flux estimation method for linear induction motors based on improved extended state observers," *IEEE Transactions on Power Electronics*, vol. 34, no. 5, pp. 4628–4640, 2019.

[10] Z. Yin, Y. Zhang, C. Du, J. Liu, X. Sun, and Y. Zhong, "Research on anti-error performance of speed and flux estimation for induction motors based on robust adaptive state observer," *IEEE Transactions on Industrial Electronics*, vol. 63, no. 6, pp. 3499–3510, 2016.

[11] J.-N. Shen, J.-J. Shen, Y.-J. He, and Z.-F. Ma, "Accurate state of charge estimation with model mismatch for li-ion batteries: A joint moving horizon estimation approach," *IEEE Transactions on Power Electronics*, vol. 34, no. 5, pp. 4329–4342, 2019.

[12] C. Alfaro, R. Guzman, L. G. de Vicuña, J. Miret, and M. Castilla, "Dual-loop continuous control set model-predictive control for a three-phase unity power factor rectifier," *IEEE Transactions on Power Electronics*, vol. 37, no. 2, pp. 1447–1460, 2022.

[13] Y. Zhang, Y. Peng, and H. Yang, "Performance improvement of two-vectors-based model predictive control of pwm rectifier," *IEEE Transactions on Power Electronics*, vol. 31, no. 8, pp. 6016–6030, 2016.

[14] C. Buccella, C. Cecati, H. Latafat, P. Pepe, and K. Razi, "Observer-based control of llc dc/dc resonant converter using extended describing functions," *IEEE Transactions on Power Electronics*, vol. 30, no. 10, pp. 5881–5891, 2015.

[15] L. Zheng, R. P. Kandula, and D. Divan, "Robust predictive control for modular solid-state transformer with reduced dc link and parameter mismatch," *IEEE Transactions on Power Electronics*, vol. 36, no. 12, pp. 14 295–14 311, 2021.

[16] Z. Zhang, F. Wang, T. Sun, J. Rodríguez, and R. Kennel, "Fpga-based experimental investigation of a quasi-centralized model predictive control for back-to-back converters," *IEEE Transactions on Power Electronics*, vol. 31, no. 1, pp. 662–674, 2016.

[17] J. Holtz, "Predictive finite-state control—when to use and when not," *IEEE Transactions on Power Electronics*, vol. 37, no. 4, pp. 4225–4232, 2022.

[18] Y. Yang, S.-C. Tan, and S. Y. R. Hui, "Adaptive reference model predictive control with improved performance for voltage-source inverters," *IEEE Transactions on Control Systems Technology*, vol. 26, no. 2, pp. 724–731, 2018.

[19] X. Liu, D. Wang, and Z. Peng, "Cascade-free fuzzy finite-control-set model predictive control for nested neutral point-clamped converters with low switching frequency," *IEEE Transactions on Control Systems Technology*, vol. 27, no. 5, pp. 2237–2244, 2019.

[20] M. Narimani, B. Wu, V. Yaramasu, Z. Cheng, and N. R. Zargari, "Finite control-set model predictive control (fcs-mpc) of nested neutral point-clamped (nnpc) converter," *IEEE Transactions on Power Electronics*, vol. 30, no. 12, pp. 7262–7269, 2015.

[21] N. Panten, N. Hoffmann, and F. W. Fuchs, "Finite control set model predictive current control for grid-connected voltage-source converters with lcl filters: A study based on different state feedbacks," *IEEE Transactions on Power Electronics*, vol. 31, no. 7, pp. 5189–5200, 2016.

[22] A. Monti and F. Ponci, "Pebb standardization for high-level control: A proposal," *IEEE Transactions on Industrial Electronics*, vol. 59, no. 10, pp. 3700–3709, 2012.

[23] T. Ericsen, Y. Khersonsky, P. Schugart, and P. Steimer, "Pebb - power electronics building blocks, from concept to reality," in *2006 3rd IET International Conference on Power Electronics, Machines and Drives - PEMD 2006*, 2006, pp. 12–16.

[24] A. Deshpande, Y. Chen, B. Narayanasamy, Z. Yuan, C. Chen, and F. Luo, "Design of a high-efficiency, high specific-power three-level t-type power electronics building block for aircraft electric-propulsion drives," *IEEE Journal of Emerging and Selected Topics in Power Electronics*, vol. 8, no. 1, pp. 407–416, 2020.

[25] H. L. Ginn, N. Hingorani, J. R. Sullivan, and R. Wachal, "Control architecture for high power electronics converters," *Proceedings of the IEEE*, vol. 103, no. 12, pp. 2312–2319, 2015.

[26] Y. Li, Y. Gu, and T. Green, "Revisiting grid-forming and grid-following inverters: A duality theory," *IEEE Transactions on Power Systems*, pp. 1–1, 2022.

[27] X. Yu, A. M. Khambadkone, H. Wang, and S. T. S. Terence, "Control of parallel-connected power converters for low-voltage microgrid—part i: A hybrid control architecture," *IEEE Transactions on Power Electronics*, vol. 25, no. 12, pp. 2962–2970, 2010.

[28] H. Wang, A. M. Khambadkone, and X. Yu, "Control of parallel connected power converters for low voltage microgrid—part ii: Dynamic electrothermal modeling," *IEEE Transactions on Power Electronics*, vol. 25, no. 12, pp. 2971–2980, 2010.

[29] P. Tøndel, T. A. Johansen, and A. Bemporad, "Evaluation of piecewise affine control via binary search tree," *Automatica*, vol. 39, no. 5, pp. 945–950, 2003.

[30] M. Herceg, M. Kvasnica, C. N. Jones, and M. Morari, "Multi-parametric toolbox 3.0," in *2013 European Control Conference (ECC)*, 2013, pp. 502–510.

[31] M. G. Judewicz, S. A. González, J. R. Fischer, J. F. Martínez, and D. O. Carrica, "Inverter-side current control of grid-connected voltage source inverters with lcl filter based on generalized predictive control," *IEEE Journal of Emerging and Selected Topics in Power Electronics*, vol. 6, no. 4, pp. 1732–1743, 2018.

[32] S. Mariethoz and M. Morari, "Explicit model-predictive control of a pwm inverter with an lcl filter," *IEEE Transactions on Industrial Electronics*, vol. 56, no. 2, pp. 389–399, 2009.

[33] C. Xue, D. Zhou, and Y. Li, "Hybrid model predictive current and voltage control for lcl-filtered grid-connected inverter," *IEEE Journal of Emerging and Selected Topics in Power Electronics*, vol. 9, no. 5, pp. 5747–5760, 2021.

[34] R. Guzman, L. G. de Vicuña, A. Camacho, J. Miret, and J. M. Rey, "Receding-horizon model-predictive control for a three-phase vsi with an lcl filter," *IEEE Transactions on Industrial Electronics*, vol. 66, no. 9, pp. 6671–6680, 2019.

[35] C. S. Lim, H. H. Goh, and S. S. Lee, "Long-prediction-horizon near-optimal model predictive grid current control for pwm-driven vsis with lcl filters," *IEEE Transactions on Power Electronics*, vol. 36, no. 2, pp. 2246–2257, 2021.

[36] N. N. Nam, N. D. Nguyen, C. Yoon, M. Choi, and Y. I. Lee, "Voltage sensorless model predictive control for a grid-connected inverter with lcl filter," *IEEE Transactions on Industrial Electronics*, vol. 69, no. 1, pp. 740–751, 2022.

[37] N. N. Nam, N.-D. Nguyen, C. Yoon, and Y. I. Lee, "Disturbance observer-based robust model predictive control for a voltage sensorless grid-connected inverter with an lcl filter," *IEEE Access*, vol. 9, pp. 109 793–109 805, 2021.

[38] B. Wang, Y. Xu, Z. Shen, J. Zou, C. Li, and H. Liu, "Current control of grid-connected inverter with lcl filter based on extended-state observer estimations using single sensor and achieving improved robust observation dynamics," *IEEE Transactions on Industrial Electronics*, vol. 64, no. 7, pp. 5428–5439, 2017.

[39] W. He, M. M. Namazi, T. Li, and R. Ortega, "A state observer for sensorless control of power converters with unknown load conductance," *IEEE Transactions on Power Electronics*, vol. 37, no. 8, pp. 9187–9199, 2022.

[40] S. Zhuo, A. Gaillard, L. Xu, D. Paire, and F. Gao, "Extended state observer-based control of dc–dc converters for fuel cell application," *IEEE Transactions on Power Electronics*, vol. 35, no. 9, pp. 9923–9932, 2020.

[41] J. Kukkola, M. Hinkkanen, and K. Zenger, "Observer-based state-space current controller for a grid converter equipped with an lcl filter: Analytical method for direct discrete-time design," *IEEE Transactions on Industry Applications*, vol. 51, no. 5, pp. 4079–4090, 2015.

[42] J. Kukkola and M. Hinkkanen, "Observer-based state-space current control for a three-phase grid-connected converter equipped with an lcl filter," *IEEE Transactions on Industry Applications*, vol. 50, no. 4, pp. 2700–2709, 2014.

[43] M. A. Awal, L. D. Flora, and I. Husain, "Observer based generalized active damping for voltage source converters with lcl filters," *IEEE Transactions on Power Electronics*, vol. 37, no. 1, pp. 125–136, 2022.

[44] R. Errouissi and A. Al-Durra, "Design of pi controller together with active damping for grid-tied lcl-filter systems using disturbance-observer-based control approach," *IEEE Transactions on Industry Applications*, vol. 54, no. 4, pp. 3820–3831, 2018.

Liwei Zhou (S'15) received the B.E. and the M.E. degrees both in electrical engineering from Shandong University, Jinan, China, in 2014 and 2017, respectively. He obtained the Ph.D. degree in electrical engineering from Columbia University, New York City, in 2022.

He is currently a research associate in Motor Drives and Power Electronics Laboratory (MPLab), Columbia University. His current research interests include soft-switching techniques for modular power converter, model predictive control, state estimation and other advanced control technologies, grid-connected converter, electric vehicle battery charging control, and inductor design. He serves as the session chair in 2022 IEEE/AIAA ITEC+EATS. He won the best paper award in the International Conference on Applied Energy, MIT A+B 2022. He was the recipient of the IEEE Energy Conversion Congress and Expo 2018 Student Travel Award. He was also the co-recipient of the Best Student Paper Award of the IEEE Transportation Electrification Conference and Expo 2021.

Michael Eull (S'12) received the B.Eng.Mgt. and MASc degrees from McMaster University, Hamilton, ON, Canada and the PhD degree from Columbia University, New York, NY, USA, all in electrical engineering. He is currently a Research and Development Engineer in power electronics at the Power Networks Demonstration Centre, University of Strathclyde, United Kingdom and is serving as the Treasurer for the 2022 IEEE/AIAA ITEC+EATS conference. His research interests are in estimation and control of power electronics and motor drives for transportation electrification.

Matthias Preindl (S'12-M'15-SM'18) received the B.Sc. degree in electrical engineering (*summa cum laude*) from the University of Padua, Italy, the M.Sc. degree in electrical engineering and information technology from ETH Zurich, Switzerland, and the Ph.D. degree in energy engineering from the University of Padua, in 2008, 2010, and 2014, respectively. He is currently Associate Professor of Power Electronic Systems in the Department of Electrical Engineering at Columbia University, USA. Prior to joining Columbia University in 2016, he was an R&D Engineer of Power Electronics and Drives at Leitwind AG, Italy (2010-2012), a Post Doctoral Research Associate with the McMaster Institute for Automotive Research and Technology, McMaster University, Hamilton, ON, Canada (2014-2015), and a Sessional Professor in the Department of Electrical and Computer Engineering, McMaster University (2015).

Dr. Preindl serves as Area Editor of IEEE Transactions on Vehicular Technology, Associate EiC of Springer Nature/China SAE Journal of Automotive Innovation, and as the general chair of the 2022 IEEE/AIAA ITEC+EATS. He is a Fellow of IET, recipient of the Horiba Awards Honorable Mention (Japan, 2019), the Futura Foundation Award (Italy, 2017), and the NSF CAREER Award (USA, 2017), co-recipient of Fast Company's World Changing Ideas Awards honorable mention (co-recipient, USA, 2022) as well as best paper and presentation recognitions including the 2019 IEEE Transactions on Industrial Electronics best paper award. His research interests include the design and control of motor drives, power electronics, and batteries for transportation electrification and renewable energy.